INTERNATIONAL JOURNAL FOR NUMERICAL METHODS IN FLUIDS
Int. J. Numer. Meth. Fluids 2006; **51**:1059–1077
Published online in Wiley InterScience (www.interscience.wiley.com). DOI: 10.1002/fld.1245

Higher-resolution hyperbolic-coupled-elliptic flux-continuous CVD schemes on structured and unstructured grids in 2-D

Michael G. Edwards*, †

Civil and Computational Engineering Centre, School of Engineering, University of Wales Swansea, Singleton Park, Swansea SA2 8PP, U.K.

SUMMARY

Higher-order convection schemes have been developed for the essentially hyperbolic systems of reservoir simulation and can significantly enhance solution quality. Locally conservative full-tensor flux-continuous finite-volume schemes have also been developed for the porous medium pressure equation with general geometry and permeability tensors on structured and unstructured grids. These schemes remove $O(1)$ errors induced by standard methods, and are now recognized as an essential component of any numerical method designed for reservoir simulation and modelling flow in porous media.

In this paper, novel higher-resolution hyperbolic conservation law schemes, designed for convective flux approximation on unstructured grids are coupled with general full-tensor continuous Darcy flux approximations. The schemes are developed for multi-phase flow in porous media. Benefits in terms of improved front resolution are demonstrated. Comparisons with current methods including the control-volume finite element (CVFE) method highlight the advantages of the new formulation for flow resolution in reservoir simulation. Copyright © 2006 John Wiley & Sons, Ltd.

Received 2 June 2005; Revised 7 February 2006; Accepted 16 February 2006

KEY WORDS: higher-order; flux-continuous; full-tensor; finite-volume; unstructured

1. INTRODUCTION

Reservoir simulation of multi-phase flow processes involves solving an essentially hyperbolic system for fluid transport coupled with an essentially elliptic system for pressure and Darcy velocity [1], see also Reference [2]. For a given geological description, the accuracy and efficiency of reservoir simulation are dependent upon the grid quality, the type of the numerical approximation for

*Correspondence to: Michael G. Edwards, Civil and Computational Engineering Centre, University of Wales Swansea, Swansea, U.K.
†E-mail: m.g.edwards@swansea.ac.uk

Contract/grant sponsor: EPSRC; contract/grant number: GR/S70968/01

both the essentially hyperbolic and elliptic differential operators, the efficiency of the solution process, and the accuracy of the upscaling algorithm. The focus here is on the numerical approximation and coupling of the essentially hyperbolic and elliptic differential operators for general grids.

Higher-order convection schemes continue to be developed for the essentially hyperbolic systems of reservoir simulation, e.g. References [3–10]. These schemes require an extended support to obtain higher-order accuracy and are constructed such that the solution remains monotonic. These methods yield benefits in terms of improved front resolution and have been successfully demonstrated for a variety of multi-phase flow problems in reservoir simulation.

Locally conservative flux-continuous full-tensor finite-volume schemes also continue to be developed for the essentially elliptic component of the reservoir simulation system [11–23]. These schemes are control-volume distributed (CVD) where flow variables and rock properties are associated with the control-volumes of the grid and provide a consistent discretization of the porous medium pressure equation applicable to general geometry and permeability tensors on structured and unstructured grids, e.g. Reference [12]. Methods of this type are also known as multi-point flux approximation schemes (MPFA) [17]. Prior to the development of CVD schemes, mixed finite element methods [6, 24–28] offered the only schemes capable of preserving flux continuity for full-tensor flows. However, mixed methods solve for velocity components and pressure in a globally coupled system and for two-dimensional structured grids involve solving for 3 times as many degrees of freedom as (the more efficient) CVD methods. In summary the CVD schemes remove $O(1)$ errors induced by standard methods in cases when full tensors are present, maintain flux continuity and retain the same number of degrees of freedom as standard schemes (i.e. one discrete pressure value per control-volume). These schemes are now recognized as an essential component of any numerical method designed for reservoir simulation and modelling flow in porous media.

In this paper, a novel higher-order scheme with local maximum principle is presented for two-dimensional unstructured grids. The higher-order convective flux approximation is coupled with consistent and efficient continuous Darcy flux approximations that are applicable on structured and unstructured grids comprised of triangles and quadrilaterals in two dimensions. The coupling of higher-order phase component approximations with the general tensor flux-continuous formalism provides an improved and novel scheme for reservoir simulation, applicable to multi-phase flow while using an optimal number of degrees of freedom within the discretization. Benefits of the resulting schemes in terms of front resolution and medium discontinuity resolution are demonstrated for two-phase flow test cases in two dimensions.

Flow equations are presented in Section 2. A summary of the flux-continuous formulation is presented in Section 3. Extension of the higher-order schemes to general unstructured grids is presented in Section 4. The flux-continuous formulation is contrasted with the control-volume finite element (CVFE) formulation [29] in Section 5 where the key advantages of the new formulation are discussed. Two-phase flow results are presented in Section 6 that demonstrate the advantages of the new higher-order flux-continuous formulation. Comparisons with current methods in reservoir simulation and with the standard control-volume finite element CVFE scheme [29], which uses exactly the same number of degrees of freedom, serve to highlight the advantages of the new formulation for reservoir simulation. Conclusions follow in Section 7.

2. FLOW EQUATIONS

Without loss of generality in terms of the numerical methods applicability, the schemes presented here are illustrated with respect to two-phase flow models, with unit porosity and where capillary

DOI: 10.1002/fld

pressure and dispersion are neglected. The integral form of the flow equations is given in anticipation of the generalization to general geometry and finite-volume discretization. In order to simplify notation gravity will be omitted from the formalism, however once the discrete flux is defined gravity can be included immediately. After integrating over a control volume Ω_{cv} with surface $\partial\Omega_{\mathrm{cv}}$ via the Gauss divergence theorem, the continuity equations for phases $p=1, N_p$ are written as

$$\int_{\Omega_{\mathrm{cv}}} \frac{\partial S_p}{\partial t} + \oint_{\partial\Omega_{\mathrm{cv}}} \mathbf{V}_p \bullet \hat{\mathbf{n}}\, \mathrm{d}s = m_p \tag{1}$$

where the integral is taken over Ω_{cv} and where S_p, $\mathbf{V}_p$ and m_p are the pth phase saturation, Darcy velocity (defined below) and specified phase flow rate, respectively. Since the pore volume must always be filled by the fluids present, this gives rise to the volume balance

$$\sum_{p=1}^{N_p} S_p = 1 \tag{2}$$

The momentum equations are defined through Darcys law where the pth phase velocity is defined by

$$\mathbf{V}_p = \mathrm{f}_p \mathbf{V}_{\mathrm{T}} \tag{3}$$

here f_p is the fractional flow of phase p and $\mathbf{V}_{\mathrm{T}}$ is the total Darcy velocity defined via

$$\mathbf{V}_{\mathrm{T}} = -\Lambda \mathbf{K} \nabla \phi \tag{4}$$

where $\Lambda = \sum_{p=1}^{N_p} \lambda_p$ is the total mobility, with pth phase mobility given by

$$\lambda_p = k_{\mathrm{rp}}/\mu_p \tag{5}$$

where μ_p and k_{rp} are the respective phase viscosity and relative permeability. $\mathbf{K}$ is a diagonal or full elliptic Cartesian permeability tensor, ϕ is the pressure and $\nabla = \partial_{x_i}$.

Neumann boundary conditions apply on solid walls with zero normal flux. Inflow–outflow conditions apply at wells where fluxes/pressures are prescribed. Initial data in terms of saturation and pressure fields are also prescribed. Further details can be found in Reference [1]. The closed surface integral of phase velocity can now be expressed as the sum of outward normal phase fluxes F_{p_i} over each of the surface increments of the control-volume Ω_{cv}, viz

$$\oint_{\partial\Omega_{\mathrm{cv}}} \mathbf{V}_p \bullet \hat{\mathbf{n}}\, \mathrm{d}s = \sum_{i=1}^{N_{\mathrm{S}}} \mathrm{F}_{p_i} \tag{6}$$

where N_{S} is the number of surface increments that enclose the volume Ω_{cv}. The outward normal phase flux in the ith normal direction is written in terms of the general tensor $\mathbf{T}$ as

$$\mathrm{F}_{p_i} = -\int_{\partial\Omega_{\mathrm{cv}}} \mathrm{f}_p \Lambda \sum_{j=1}^{N_{\mathrm{D}}} T_{ij} \phi_{\xi_j}\, \mathrm{d}\Gamma_i \tag{7}$$

where ξ_i are local curvilinear parametric coordinates, Γ_i is the parametric coordinate surface increment and ϕ_{ξ_j} is the derivative of ϕ with respect to ξ_j and

$$\mathbf{T} = J\mathbf{J}^{-1}\mathbf{K}\mathbf{J}^{-\mathrm{T}} \tag{8}$$

DOI: 10.1002/fld

is the general tensor defined via the Piola transformation which is function of the Cartesian permeability tensor and geometry, where $J_{ij} = \partial x_i / \partial \xi_j$ is the Jacobian of the local curvilinear coordinate transformation. The grids considered here generally give rise to non-zero cross terms with $T_{ij} \neq 0$ for $i \neq j$ in the general tensor. Full tensors can arise from upscaling, and orientation of grid and permeability field. For example, by Equation (7), a diagonal anisotropic Cartesian tensor leads to a full tensor on a curvilinear *orthogonal* grid. In two dimensions the general tensor coefficients take the form

$$\begin{aligned} T_{11} &= (K_{11} y_\eta^2 + K_{22} x_\eta^2 - 2K_{12} x_\eta y_\eta)/J \\ T_{22} &= (K_{11} y_\xi^2 + K_{22} x_\xi^2 - 2K_{12} x_\xi y_\xi)/J \\ T_{12} &= (K_{12}(x_\xi y_\eta + x_\eta y_\xi) - (K_{11} y_\eta y_\xi + K_{22} x_\eta x_\xi)/J \end{aligned} \tag{9}$$

where $J = x_\xi y_\eta - y_\xi x_\eta$ is the Jacobian determinant. For incompressible flow Equation (1) is summed over the N_p phases and Equation (2) is used to yield the pressure equation

$$\sum_{i=1}^{N_S} \mathrm{F}_{T_i} = 0 \tag{10}$$

away from sources and sinks (or wells) where the total flux F_{T_i} involves a product of total mobility and single-phase flow flux and is given by

$$\mathrm{F}_{T_i} = -\int_{\partial\Omega_{cv}} \Lambda \sum_{j=1}^{N_D} T_{ij} \phi_{\xi_j} \, \mathrm{d}\Gamma_i \tag{11}$$

and N_D is the dimension number.

3. FLUX-CONTINUOUS CONTROL-VOLUME DISTRIBUTED (CVD) APPROXIMATIONS

A given primal grid is comprised of elements, or cells, with corners defined by the grid vertices. After generating the grid, there is a choice to be made in flow and rock variable representation. In reservoir simulation flow and rock variables are always CVD. Thus, the choice is between distributing flow and rock variables to vertex-centred control-volumes, where polygonal control-volumes are built around the grid vertices (described below see *Continuous Flux Approximation in Higher Dimensions*) or distributing variables to cell centres where primal grid cells act as the control-volumes. In the cell-centred case a dual grid is then constructed in order to construct the local flux continuity constraints. In the formulation presented here the former (vertex-centred) option is selected. While cell-centred schemes for reservoir simulation are common [1, 15–18, 22, 23], their generalization to the quite general grid types considered here are still under development and will form the subject of future work.

The schemes presented here are therefore vertex centred, derived in a CVD framework, where for a given control-volume surrounding a grid vertex, flow variables are assigned to grid vertices *and* rock properties are piecewise constant with respect to the control-volumes. The physical constraints that must be enforced are continuity of pressure and continuity of normal flux across interfaces (control-volume faces) that separate changes in permeability tensor.

DOI: 10.1002/fld

3.1. Continuous flux approximation in one dimension

Before introducing higher-dimensional Darcy flux approximation schemes we will recap on the basic principles that govern the derivation of the most classical and common one-dimensional schemes employed in reservoir simulation [1, 12]. Consider a grid of nodes in one spatial dimension. Primal grid cells are defined by the intervals between nodes or vertices with index i. Control-volume faces are defined by the interval mid-points and a control-volume surrounds each vertex in the domain. The integral of the one-dimensional pressure equation over a control-volume reduces to the difference of fluxes at the interfaces

$$-((K\phi_x)_{i+1/2} - (K\phi_x)_{i-1/2}) = 0 \tag{12}$$

and an appropriate approximation of flux $-(K\phi_x)_{i+1/2}$ at interface $i + 1/2$ must now be constructed at each interface. A discrete value of permeability K_i and pressure ϕ_i is assigned to each control-volume. The continuity constraints are built into the scheme by a sub-cell flux construction. The first step involves introducing temporary interface pressures ϕ_f on the control-volume faces that separate changes in permeability and give rise to a continuous variation in discrete pressure. The approximate pressure field then assumes a piecewise linear sub-cell variation between the vertex and continuous interface pressures.

The second step involves the actual sub-cell flux reconstruction where piecewise constant sub-cell fluxes are defined on the left- and right-hand sides of each control-volume interface. Pressure and flux continuity conditions are imposed by equating fluxes on the left- and right-hand sides of the interface to arrive at one local equation for each discrete cell face pressure viz:

$$-K_i(\phi_f - \phi_i)/(h/2) = -K_{i+1}(\phi_{i+1} - \phi_f)/(h/2) \tag{13}$$

From which it follows that the cell face pressure can be expressed as a linear combination of the adjacent cell vertex pressures in an *a priori* elimination step, viz

$$\phi_f = (K_i\phi_i + K_{i+1}\phi_{i+1})/(K_i + K_{i+1}) \tag{14}$$

Upon back substitution into Equation (13) the well-known approximation for single phase flux at an interface is obtained, and is given by the product of discrete pressure gradient multiplying the harmonic mean of adjacent cell permeabilities.

$$F_{i+1/2} = -2K_iK_{i+1}(\phi_{i+1} - \phi_i)/(K_i + K_{i+1})h \tag{15}$$

3.2. Continuous flux approximation in two dimensions

In this section, we shall first focus on approximation of the incompressible single-phase flow equation and present an overview of the flux-continuous formulation [12]. The primal grid considered here can be a hybrid composed of triangles and/or quadrilateral cells in two dimensions with no restriction on structure. A polygonal control-volume is built around each grid vertex by joining (triangular or quadrilateral) cell centres with cell edge mid-points in (two dimensions) Figure 1, for all cells that share a common grid vertex. The resulting set of polygonal control-volumes defines a dual grid relative to the primal grid. The construction of the dual grid can also be viewed as a decomposition of primal grid cells in to sub-quadrilateral cells in two dimensions, three for a triangle, four for a quadrilateral. The decomposition is followed by a local assembly or recomposition

DOI: 10.1002/fld

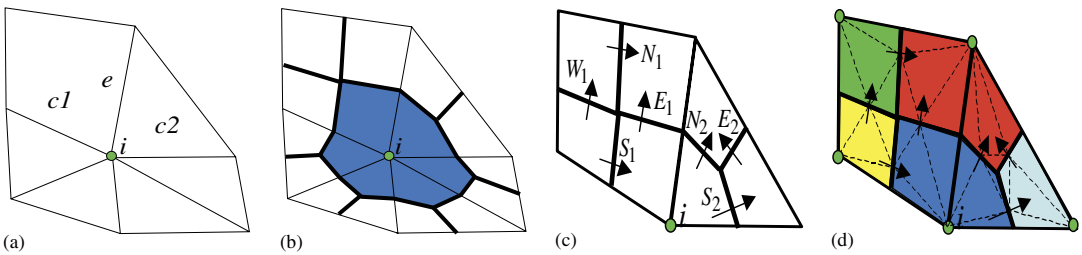

Figure 1. (a) Segment of primal grid; (b) control-volume; (c) dual grid (bold) and fluxes in cells c1 and c2; and (d) sub-cell flux basis (dotted triangles).

at each primal grid vertex of all sub-cells that are attached to the vertex, Figure 1(b). Rock permeability and porosity are assumed to be piecewise constant over each polygonal control-volume Figure 1(b), thus rock properties can therefore be discontinuous over the control-volume faces.

The finite-volume formulation begins with the integral form of the flow equations, c.f. Equation (1). The Gauss divergence theorem is applied to the integral of divergence locally over each control-volume. A unique discrete flux is then constructed for each control-volume face (see below) and the closed integral of flux is approximated by the sum of discrete outward normal fluxes. For a given face that is common to two neighbouring control-volumes, a unique flux is subtracted from the left-hand control-volume while the same flux is added to the right-hand control-volume. Consequently, the discrete integral form of the flow equations is locally conservative with a summation over all control-volumes leaving only the sum of global domain boundary (outward normal) fluxes. Thus, the schemes considered here are locally conservative over the faces of the polygonal control-volumes that contain the discrete permeability tensors with flow variables defined at their vertices.

In this formulation, the construction of the elliptic finite-volume scheme begins by building fluxes on the sub-cell faces that lie inside a primal grid cell [12]. For example, for a quadrilateral primal grid cell c_1, Figure 1(a) the interior sub-cell faces are labelled $(\mathrm{N}_1, \mathrm{S}_1, \mathrm{E}_1, \mathrm{W}_1)$ to indicate the North, South, East and West cell faces locations. Fluxes are defined along the normal to each control-volume sub-cell face inside the primal quadrilateral cell, Figure 1(c), leading to the four sub-cell fluxes

$$F_{\mathrm{N}_1}, F_{\mathrm{S}_1}, F_{\mathrm{E}_1}, F_{\mathrm{W}_1} \tag{16}$$

while for the triangular cell c_2 there are three sub-cell fluxes,

$$F_{\mathrm{N}_2}, F_{\mathrm{S}_2}, F_{\mathrm{E}_2} \tag{17}$$

as indicated in the triangle of Figure 1(c). The derivation of the (continuous) fluxes is summarized in the next subsection. Each sub-cell flux is associated with a unique cell edge and once defined, the sub-cell fluxes are accumulated with respect to their cell edges within an assembly process. The edge index $e(i, j)$ refers to the jth edge attached to vertex i. The net edge-based single phase flux $F_{e(i,j)}(\phi)$ associated with edge $e(i, j)$ is comprised of the sum of adjacent sub-cell fluxes that belong to the primal grid cells with common edge $e(i, j)$. For example, in a two-dimensional domain interior two adjacent sub-cell fluxes are assembled for each cell edge. This is illustrated with reference to vertex i and local edge e of Figure 1(a) and the local fluxes of Figure 1(c), in

DOI: 10.1002/fld

this case the net edge-based flux is given by

$$F_{e(i,j)} = F_{\mathrm{E}_1} + F_{\mathrm{N}_2} \tag{18}$$

After assembly of net edge-based fluxes, the discrete scheme for each vertex i is completed with the closed integral of net Gaussian flux approximated by the sum of the net edge-based fluxes corresponding to edges connected to the ith vertex.

For single-phase flow on unstructured grids the assembled finite-volume scheme at vertex i can be written concisely as

$$\sum_{j=1}^{N_{\mathrm{ed}V}} F_{e(i,j)}(\phi) = M_i \tag{19}$$

where summation is over all $N_{\mathrm{ed}V}$ edges passing through the ith grid vertex, (M_i denotes a specified flow rate at vertex i, or is zero otherwise).

3.3. Control-volume flux and continuity

For the CVD cell-vertex formulation, in higher dimensions a consistent normal flux approximation is constructed that respects continuity of pressure and flux across the control-volume interfaces within each primal grid cell. For a quadrilateral cell of the primal grid, this is achieved by introducing four auxiliary continuous interface pressures $\mathbf{\Phi}_{\mathrm{f}} = (\phi_{\mathrm{N}}, \phi_{\mathrm{S}}, \phi_{\mathrm{E}}, \phi_{\mathrm{W}})$, one per control-volume sub-face as indicated in Figure 1(c). Four sub-cell triangular basis functions are then formed by joining the cell vertices (with locally numbered vertex pressures (anti-clockwise, lower left hand vertex is 1) $\mathbf{\Phi}_{\mathrm{v}} = (\phi_1, \phi_2, \phi_3, \phi_4)$) to the positions of the adjacent interface pressures Figure 1(d), and eight sub-cell normal fluxes are defined, two per triangle. Flux continuity is then imposed by equating fluxes on the left- and right-hand sides of each of the four interfaces resulting in

$$\begin{aligned}
F_{\mathrm{N}} &= -\tfrac{1}{2}(T_{11}\phi_\xi + T_{12}\phi_\eta)|^4_{\mathrm{N}} = -\tfrac{1}{2}(T_{11}\phi_\xi + T_{12}\phi_\eta)|^3_{\mathrm{N}} \\
F_{\mathrm{S}} &= -\tfrac{1}{2}(T_{11}\phi_\xi + T_{12}\phi_\eta)|^1_{\mathrm{S}} = -\tfrac{1}{2}(T_{11}\phi_\xi + T_{12}\phi_\eta)|^2_{\mathrm{S}} \\
F_{\mathrm{E}} &= -\tfrac{1}{2}(T_{12}\phi_\xi + T_{22}\phi_\eta)|^2_{\mathrm{E}} = -\tfrac{1}{2}(T_{12}\phi_\xi + T_{22}\phi_\eta)|^3_{\mathrm{E}} \\
F_{\mathrm{W}} &= -\tfrac{1}{2}(T_{12}\phi_\xi + T_{22}\phi_\eta)|^1_{\mathrm{W}} = -\tfrac{1}{2}(T_{12}\phi_\xi + T_{22}\phi_\eta)|^4_{\mathrm{W}}
\end{aligned} \tag{20}$$

where the general tensor $\mathbf{T}$ of Equation (9) is approximated locally by resolving physical full-tensor fluxes with respect to the sub-cell geometry and control-volume permeability. The discrete pressure field has a piecewise linear variation over each sub-cell triangle c.f. Figure 1(d), and consequently approximations of the derivatives ϕ_ξ, ϕ_η are linear functions of $\mathbf{\Phi}_{\mathrm{f}}$ and $\mathbf{\Phi}_{\mathrm{v}}$. Here $\Gamma\,|^j_\sigma$ denotes interface flux Γ at location σ and state of volume j. The actual position of σ along each sub-cell face defines both the point of continuous pressure and the flux quadrature (Figure 1(c)), and in turn leads to a family of schemes as shown in Reference [16]. The effect of quadrature point upon accuracy is explored in the convergence study of two-dimensional single-phase flow problems on cell-centred quadrilateral grids and polygonal vertex-centred grids is presented in Reference [30].

DOI: 10.1002/fld

The flux continuity formulation carries over directly to triangular cells [12, 14, 19–21]. In this case, three flux continuity conditions are imposed within each triangle and are expressed as

$$\begin{aligned} F_{\mathrm{N}} &= \tfrac{1}{2}(T_{12}\phi_\xi + T_{22}\phi_\eta)|_{\mathrm{N}}^1 = -\tfrac{1}{2}(T_{11}\phi_\xi + T_{12}\phi_\eta)|_{\mathrm{N}}^3 \\ F_{\mathrm{S}} &= -\tfrac{1}{2}(T_{11}\phi_\xi + T_{12}\phi_\eta)|_{\mathrm{S}}^1 = -\tfrac{1}{2}(T_{11}\phi_\xi + T_{12}\phi_\eta)|_{\mathrm{S}}^2 \\ F_{\mathrm{E}} &= -\tfrac{1}{2}(T_{12}\phi_\xi + T_{22}\phi_\eta)|_{\mathrm{E}}^2 = -\tfrac{1}{2}(T_{12}\phi_\xi + T_{22}\phi_\eta)|_{\mathrm{E}}^3 \end{aligned} \tag{21}$$

where a local coordinate system is associated with each sub-cell of a given triangle, Figure 1. Interface pressures $\mathbf{\Phi}_{\mathrm{f}} = (\phi_{\mathrm{N}}, \phi_{\mathrm{S}}, \phi_{\mathrm{E}})$ are introduced on the sub-quadrilateral boundaries in a similar fashion, and three sub-cell triangular basis functions are formed by joining vertices with pressures $\mathbf{\Phi}_{\mathrm{v}} = (\phi_1, \phi_2, \phi_3)$ to adjacent interfaces with pressures $\mathbf{\Phi}_{\mathrm{f}}$. As before, the pressure assumes a piecewise linear variation over each sub-cell triangle and the derivatives ϕ_ξ, ϕ_η are linear functions of $\mathbf{\Phi}_{\mathrm{f}}$ and $\mathbf{\Phi}_{\mathrm{v}}$. The symbol $\Gamma\ |_\sigma^j$ denotes interface flux Γ at location σ and state of volume j as above. Further schemes which have symmetric positive definite matrices for single-phase flow are presented in References [11, 12, 31].

The systems of fluxes of Equations (20) and (21) are rearranged in the form

$$\mathbf{F} = A_{\mathrm{L}}\mathbf{\Phi}_{\mathrm{f}} + B_{\mathrm{L}}\mathbf{\Phi}_{\mathrm{v}} = A_{\mathrm{R}}\mathbf{\Phi}_{\mathrm{f}} + B_{\mathrm{R}}\mathbf{\Phi}_{\mathrm{v}} \tag{22}$$

and thus the interface pressures can be expressed *locally* in terms of the cell vertex pressures, leading to a generalization of Equations (13)–(15). After elimination of the $\mathbf{\Phi}_{\mathrm{f}}$ from Equation (22) it follows that

$$\mathbf{F} = (A_{\mathrm{L}}(A_{\mathrm{L}} - A_{\mathrm{R}})^{-1}(B_{\mathrm{R}} - B_{\mathrm{L}}) + B_{\mathrm{L}})\mathbf{\Phi}_{\mathrm{v}} \tag{23}$$

Convergence of the method has been verified by experiment [16, 30, 32]. The fluxes of Equation (23) can also be written as a linear combination of cell-edge potential differences [12], demonstrating the consistency condition that flux is zero for constant potential and each component of flux takes the form

$$F_\sigma(\phi) = -\frac{1}{2}\sum_{j=1}^{N\mathrm{ed}C} \alpha_j^\sigma \Delta_j \phi \tag{24}$$

where $N\mathrm{ed}C$ is the number edges of the primal grid cell. Further details of the formulations are given in References [12–16].

4. HIGHER-ORDER MULTI-PHASE FLOW APPROXIMATIONS

The general finite-volume discretization of Equation (1) for multi-phase flow on unstructured grids takes the form

$$(S_{p_i}^{n+1} - S_{p_i}^n)\tau_i + \Delta t \sum_{j=1}^{N_{\mathrm{ed}V}} \mathrm{f}_p(\mathbf{S}_{\mathrm{L}}^{n+q}, \mathbf{S}_{\mathrm{R}}^{n+q}) F_{T_{e(i,j)}}(\phi^{n+1}) = \Delta t M_{p_i} \tag{25}$$

for the pth phase continuity equation, where $\mathbf{S}_{\mathrm{L}}^{n+q}, \mathbf{S}_{\mathrm{R}}^{n+q}$ are the left- and right-hand values of the phase saturation vectors with respect to edge $e(i, j)$ and $n + q$ denotes the time level of the

DOI: 10.1002/fld

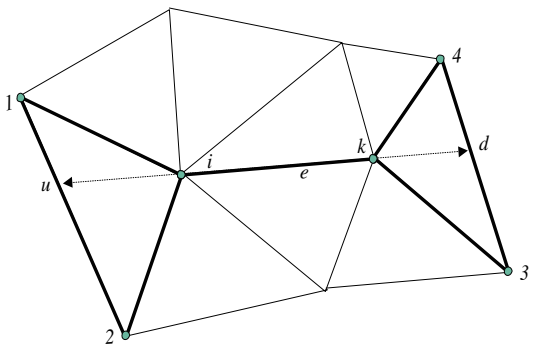

Figure 2. Higher-order support.

scheme. Here $F_{T_{e(i,j)}} = \Lambda F_{e(i,j)}(\phi)$ and M_{p_i} denotes the pth phase flow rate, prescribed at wells and is zero otherwise. The phase continuity equations are coupled through the discrete pressure equation

$$\sum_{j=1}^{N_{\mathrm{ed}V}} \Lambda(\mathbf{S}_{\mathrm{L}}^{n+q}, \mathbf{S}_{\mathrm{R}}^{n+q}) F_{e(i,j)}(\phi^{n+1}) = M_i \tag{26}$$

The system Equations (25) and (26) are either solved sequentially with $q = 0$ corresponding to implicit pressure explicit saturation (IMPES), or fully implicitly with $q = 1$ leading to a fully coupled implicit formulation. Note that for constant total mobility Λ the pressure equation Equation (26) reduces to the single phase pressure equation Equation (19). The approximate flux is defined according to the sign of the local wave direction w_p, evaluated here at the edge mid-point. Referring to Figure 2, with respect to a local frame of reference aligned with the direction i to k along the edge vector $\Delta\mathbf{r}_{i,k}$, the standard reservoir simulation upwind scheme is written as

$$\mathrm{f}_p(\mathbf{S}_{\mathrm{L}}^{n+q}, \mathbf{S}_{\mathrm{R}}^{n+q}) = \begin{cases} \mathrm{f}_p(\mathbf{S}_{\mathrm{L}}^{n+q}) & w_p \geqslant 0 \\ \mathrm{f}_p(\mathbf{S}_{\mathrm{R}}^{n+q}) & w_p < 0 \end{cases} \tag{27}$$

and the first-order upwind scheme, (known as single-point upstream weighting in the reservoir simulation literature [1]) is defined with $\mathbf{S}_{\mathrm{L}}^{n+q} = \mathbf{S}_i^{n+q}$ and $\mathbf{S}_{\mathrm{R}}^{n+q} = \mathbf{S}_k^{n+q}$.

4.1. Higher-order scheme

A higher-order approximation is now introduced with respect to the saturation variables. (For the remainder of this section superfix $n + q$ is omitted and it is understood that all saturations are computed at level $n + q$ depending on the choice of scheme formulation.) The scheme is expressed as a two-step process.

Higher-order states are defined by extending the MUSCL formalism [33] to higher dimensions. The procedure involves calculating higher-order left- and right-hand side states relative to the mid-point of each edge e (along which flux is to be defined) by expansions about the edge vertices at i and k, Figure 2. As in one dimension, the expansions are constrained with slope limiters to

DOI: 10.1002/fld

ensure that the higher-order data satisfy a local maximum principle, preventing the introduction of spurious extrema. First we define the difference in $\mathbf{S}$ over the edge e Figure 2, as

$$\Delta\mathbf{S}_{ki} = \mathbf{S}_k - \mathbf{S}_i \tag{28}$$

where it is now understood that $\Delta\mathbf{S}$ with a double suffix denotes a difference in $\mathbf{S}$. Referring to Figure 2 the left and right states $\mathbf{S}_\mathrm{L}$ and $\mathbf{S}_\mathrm{R}$ at the mid-point of the *key* edge e (joining vertices i and k) are expressed as

$$\mathbf{S}_\mathrm{L} = \mathbf{S}_i + \tfrac{1}{2}\Phi^+\Delta\mathbf{S}_{ki} \tag{29}$$

where Φ^+ is a function of

$$\mathbf{r}_{ki}^+ = (\Delta\mathbf{S}_{iu}/\Delta\mathbf{S}_{ki}) \tag{30}$$

and

$$\mathbf{S}_\mathrm{R} = \mathbf{S}_k - \tfrac{1}{2}\Phi^-\Delta\mathbf{S}_{ki} \tag{31}$$

where Φ^- is a function of

$$\mathbf{r}_{ki}^- = (\Delta\mathbf{S}_{dk}/\Delta\mathbf{S}_{ki}) \tag{32}$$

The differences $\Delta\mathbf{S}_{iu}$ and $\Delta\mathbf{S}_{dk}$ are well defined on a structured grid, where the locations of $\mathbf{S}_u$ $\mathbf{S}_d$ would correspond to the next upstream and downstream nodes of the grid, respectively. However, extension to unstructured grids requires special construction of the differences $\Delta\mathbf{S}_{iu}$ and $\Delta\mathbf{S}_{dk}$.

Directional differences are constructed by extrapolating along the *key* edge defined by vector $\Delta\mathbf{r}_{ki}$ in the respective upstream and downstream directions, see arrows in Figure 2. Here, the procedure is illustrated for a triangular mesh.

Extrapolation of the respective upstream and downstream data is constrained such that positivity holds for a scalar equation. The upstream triangle $i, 1, 2$ is labelled T_U and the down stream triangle $k, 3, 4$ is labelled T_D. The space vector corresponding to edge e ($d\mathbf{r}_{ki}$) is extrapolated into the respective triangles T_U, T_D, see arrows in Figure 2. This is illustrated further with respect to vertex i. The edge vector is extrapolated to the point of intersection u, on the opposite edge of the triangle T_U, Figure 2. The *upwind* difference is then obtained via the expansion

$$\Delta\mathbf{S}_{iu} = \nabla\mathbf{S}_{T_\mathrm{U}} \cdot d\mathbf{r}_{iu} \tag{33}$$

and for a linear approximation of $\mathbf{S}$ over the triangle T_U the right-hand side of Equation (33) is equal to the convex average of triangle edge differences with

$$\Delta\mathbf{S}_{iu} = (1 - \xi)\Delta\mathbf{S}_{i1} + \xi\Delta\mathbf{S}_{i2} \tag{34}$$

where $1 - \xi \geqslant 0$ and $\xi \geqslant 0$ is the ratio of area of sub-triangle $i, 1, u$ to area of triangle T_U. In order to impose a maximum principle with respect to T_U and edge e, the limiter Φ^+ is defined by

$$\Phi^+ = \phi(r_{ki}^+) \tag{35}$$

where r_{ki}^+ is defined by Equation (32) and $\phi(r)$ is any classical slope limiter [33, 36]. The higher order reconstruction is then bounded between $\mathbf{S}_k$ and $\mathbf{S}_u$. By convexity (Equation (34))

DOI: 10.1002/fld

$\mathbf{S}_u = (1-\xi)\mathbf{S}_1 + \xi\mathbf{S}_2$, thus bounds are such that

$$\min_{T_U \cup e}\{\mathbf{S}\} \leqslant \mathbf{S}_L \leqslant \max_{T_U \cup e}\{\mathbf{S}\} \tag{36}$$

over triangle T_U and edge e yielding a local maximum principle with reconstruction reducing to first order locally at two dimensional extrema.

In cases where coincidence or near coincidence is detected between the extrapolated edge and an upwind triangle edge the limiting is collapsed to be entirely edge based. A similar convex average interpolant is constructed with respect to vertex k for $\mathbf{S}_d$, using the right hand bold triangle T_D, together with analogous limiter bounds that now depend on $\phi(r_{ki}^{-})$ and the edge slopes $\Delta\mathbf{S}_{ki}$, $\Delta\mathbf{S}_{3k}$ and $\Delta\mathbf{S}_{4k}$, ensuring a maximum principle with $\min\{\mathbf{S}\} \leqslant \mathbf{S}_R \leqslant \max\{\mathbf{S}\}$ over T_D and edge e.

This scheme is essentially local edge diminishing (LED) in motivation [34, 35], but the higher-order reconstruction is applied to the data, in this work the saturation field. This completes the definition of the higher-order states. The second step of the scheme uses the upwind flux where each higher-order approximation of phase saturation is upwinded according to the direction of the phase wave speed, using Equations (29) and (31) in Equation (27). Any one of a number of limiters could be used, here limiting is based on the van-Leer limiter

$$\Phi(r) = \max\left(0, \min\left(2r, 2, \frac{(1+r)}{2}\right)\right) \tag{37}$$

Further details on limiters are presented in Reference [36] and general discussion of higher-order schemes is presented in Reference [37]. An implicit formulation is employed here. Implicit flux-limiting schemes for reservoir simulation were first presented in Reference [4], where a weighted Crank–Nicholson scheme is developed. A formal analysis of the implicit properties of the schemes presented here together with a study for arbitrary unstructured grid distortion is beyond the scope of the paper. An IMPES formulation could also be employed. Time accuracy of the methods is still under development. A common approach is the use of the Runge–Kutta method [38] for the explicit time integration of the convective equations. Note as before, that the first-order flux is recovered locally if the limiters are set to zero. A three-dimensional extension of this scheme is presented in Reference [39].

5. FLUX-CONTINUOUS CVD AND CONTRAST WITH CVFE

In contrast to the above CVD schemes where flow variables and rock properties are assigned to the control-volumes, the CVFE formulation assigns flow variables to the vertices and rock properties to the cells or elements. The CVFE formulation is not flux continuous in general and it is well known that this type of approximation can cause spreading of information when rapid changes in rock properties occur, e.g. References [40, 41]. The spreading effect can be understood by considering a checker board variation in (diagonal isotropic) permeability over a square domain and imposing a uniform (horizontal) pressure drop across the domain, with solid wall conditions at the top and bottom. If the white squares are assigned zero permeability, there should be no flow through the domain due to the symmetry of the problem. However, the CVFE scheme permits a mean non-zero flux, since by definition permeability is assigned to the cells and pressures are defined on cell corners, and a non-zero mean (arithmetic) flux arises that is proportional to the product of cell permeability multiplying cell-edge pressure differences. The exact homogenized

DOI: 10.1002/fld

permeability for this case is given by the geometric mean which is zero [42]. While the convergence of the CVFE scheme in the limit under mesh refinement is well known [43], this example illustrates the inherent spreading of flow information due to the CVFE approximation for any grid of finite scale.

The correct flow behaviour is faithfully replicated by the flux-continuous CVD schemes presented above for any grid level. In this case, the squares are the control-volumes and the most primitive diagonal tensor flux applies, proportional to pressure difference multiplying the harmonic mean of permeability, which is zero. The examples that follow in the next section illustrate this fundamental difference in behaviour between CVD and CVFE. The examples also show that while higher-order fluid transport approximations can improve a low-order result, the higher-order schemes do not compensate for the loss of information inherent in the CVFE Darcy flux.

6. RESULTS

The test cases involve two-phase flow (oil–water) initial oil saturation is prescribed and water is injected. Water saturation contours are shown in each case. Solid wall (zero normal flow) boundary conditions are applied on all exterior boundaries of each reservoir domain. The grids employed in these cases are smooth. In all cases flow rate is specified at the (inflow) injector and pressure is prescribed at the (outflow) producer.

6.1. Case 1

The first case is a study of grid orientation induced by a triangular grid shown in Figure 3. The permeability tensor is assumed to be diagonal isotropic so that the pressure field is essentially Laplacian in this case. Injection and production wells are located half-way along opposite sides of the rectangular domain, Figure 3 water saturation contours are shown at 0.25 pore volumes PV injected, Figure 4. The first result Figure 4(a) shows the effect of employing a two-point Darcy flux approximation and first-order upwind scheme for the convective flux. This is still the most commonly used method in reservoir simulation. The two-point Darcy flux introduces an $O(1)$ error in flux [14] due to the non-orthogonality of the grid in this case. The result obtained with

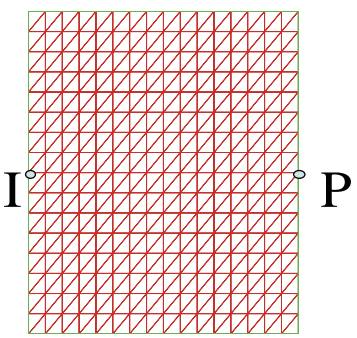

Figure 3. Triangular grid orientation study.

DOI: 10.1002/fld

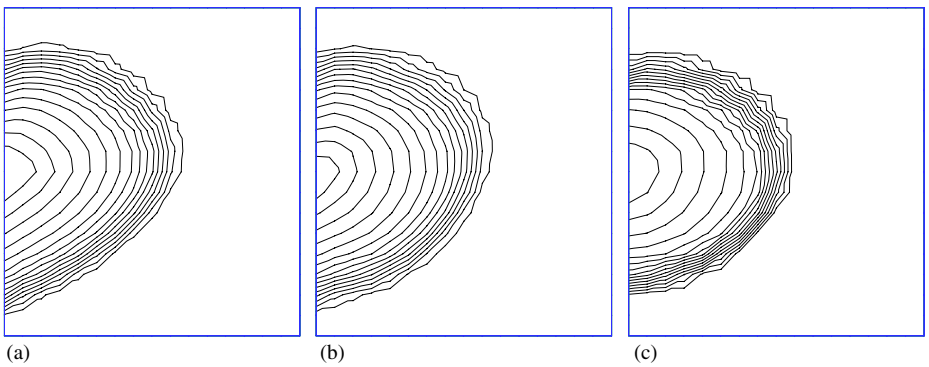

Figure 4. (a) Two-point Darcy flux—first order; (b) consistent Darcy flux—first order; and (c) consistent Darcy flux—higher order.

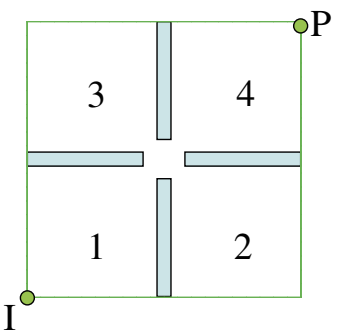

Figure 5. Quarter five-spot cascade and boundary conditions.

a consistent Darcy flux approximation and first-order convective flux is shown in Figure 4(b). While the scheme is consistent and the solution shows slightly more symmetry in contour profile than the previous scheme with in result Figure 4(a), the front still retains a bias in the direction of triangulation indicating that some grid influenced orientation remains. The result obtained with a consistent Darcy flux approximation and higher-order convective flux is shown in Figure 4(c). The higher-order scheme provides considerable improvement in resolution of the Buckley Leverett shock front and expansion together with an almost symmetric profile. The results demonstrate the need for both a consistent Darcy flux approximation and higher-order convective flux.

6.2. Case 2

The second case involves a high-permeability domain divided by four non-intersecting low-permeability barriers (with drop by six orders of magnitude in permeability) aligned in the shape of a cross, Figure 5 the configuration permits flow to be channelled through the mid-section. The permeability tensor field is defined to be diagonal isotropic in the lower-left- and top-right-hand domains (Sections 1 and 4) and a full permeability tensor is imposed in the lower-right- and

DOI: 10.1002/fld

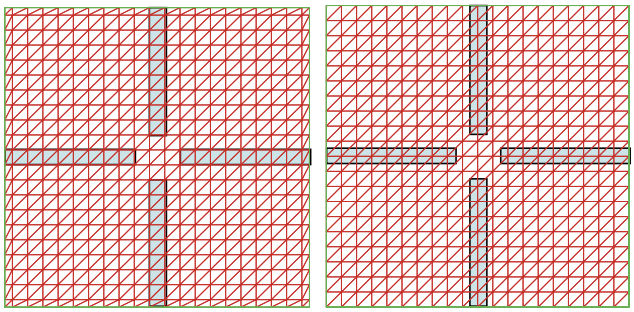

Figure 6. (a) CVFE grid; and (b) CVD grid.

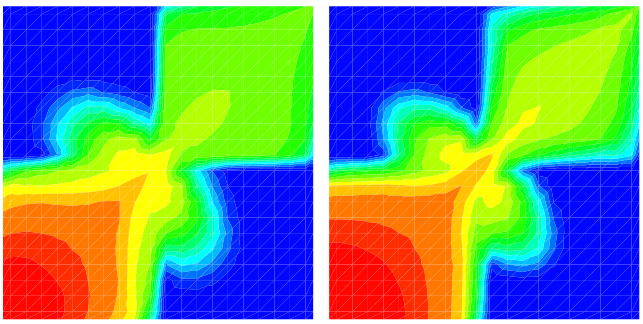

Figure 7. (a) CVFE first order; and (b) CVFE higher order.

upper-left-hand domains (Sections 2 and 3) with principal axes at 45° to the domain axes and larger principal value (ratio 9:1) along the orthogonal to the right-hand diagonal of the domain. Standard quarter five-spot boundary conditions are imposed with an injector and producer placed at the bottom-left- and top-right-hand corners, respectively. The low-permeability barriers induce a cascade effect in the usual quarter five-spot configuration. This causes the first and fourth quarter domains to effectively act as a sequence of quarter five-spot configurations, as the flow exits the first region (produced) it enters the fourth quarter of the domain (injected) so that the expected flow pattern is a repeated quarter five-spot configuration in sequence.

The low- and higher-order CVD schemes are compared with the low- and higher-order CVFE schemes for this case at 0.95 PV injected using the grids shown in Figure 6(a) and (b). The grids have been chosen so as to maintain the same problem and permeability variation with respect to the scheme formulations. The CVFE grid of Figure 6(a) shows that the permeability is defined cellwise over the triangles, while the CVD grid shows that permeability is assigned to control-volumes. First- and higher-order CVFE results are shown in Figure 7 and the respective CVD results are shown in Figure 8.

The first-order CVFE scheme is showing strong flow across the low-permeability barriers particularly near the domain centre. The CVFE saturation contours also indicate flow into the second and third quarter sections of the domain, which should remain essentially no-flow regions in this

DOI: 10.1002/fld

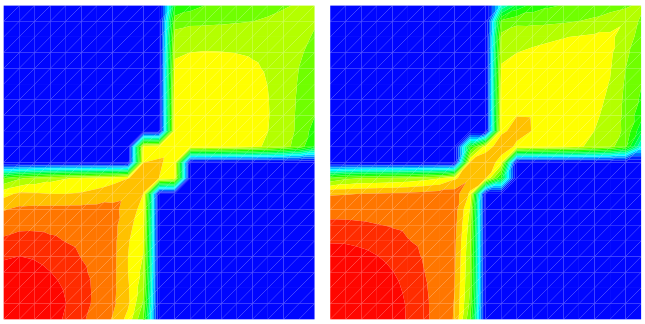

(a) (b)

Figure 8. (a) CVD first order; and (b) CVD higher order.

problem. This flow is being partly induced by the effect of the full tensor in that region. In sharp contrast, the resolution of the front in the neighbourhood of the low-permeability barriers is evident in the case of the first-order CVD scheme Figure 8(a), the CVD scheme provides much clearer resolution of flow near the low-permeability barriers with little sign of flow into the no-flow regions (second and third domain sections) in this problem.

While the higher-order CVFE scheme yields sharper shock fronts than the first-order CVFE scheme Figure 7(b), the higher-order scheme cannot compensate for the basically incorrect trend in flow behaviour predicted by the CVFE scheme. The averaging effect that is inherent in the CVFE formulation induces flow across the low-permeability barriers despite the use of a higher-order convective flux approximation. Consequently, while shocks are sharper the fronts are in the wrong physical location.

The higher-order CVD scheme provides further improvement in resolution of the shock fronts compared to the first-order CVD scheme Figure 8. The low-permeability barriers are clearly detected by the higher-order CVD scheme and the computed fronts conform to the expected quarter five-spot 'cascade'. The difference between higher-order CVD and higher-order CVFE highlights the benefits of the CVD formulation which uses the same number of degrees of freedom for flow variable approximation.

6.3. Case 3

The third case involves a heterogeneous permeability field [44], Figure 9(a). The primal (flow-based) unstructured grid ([12]) composed of quadrilaterals and triangles is shown in Figure 9(b). While the same quadrilateral-triangular grid of vertex flow variables is used for both the CVD and CVFE schemes, the permeability field is upscaled to the primal grid cells for the CVFE scheme and upscaled to the polygonal control-volumes for the CVD scheme. The CVD grid of polygonal control-volumes (dual grid in bold) with permeability distribution is shown in Figure 10, overlaying the primal grid. The boundary conditions are indicated in Figure 9(a). All results are shown at 0.4 pv injected. The result obtained with the first-order CVFE scheme is shown in Figure 11(a) and the corresponding result using the first-order CVD scheme is shown in Figure 11(b). In this case flow is largely confined along predominantly channelled paths leading to a smaller difference in character between solutions. However, the CVFE result (Figure 11(a)) is still more spread across high permeability channels, compared to the continuous Darcy-flux CVD scheme result in Figure 11(b).

DOI: 10.1002/fld

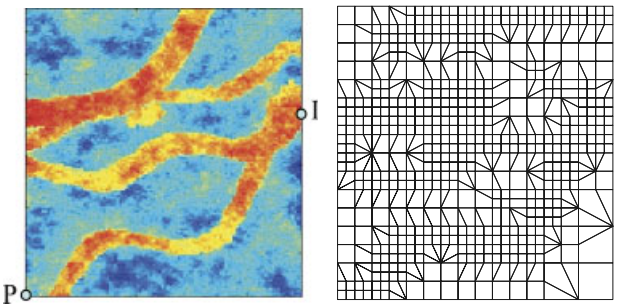

Figure 9. (a) Permeability field; and (b) primal grid.

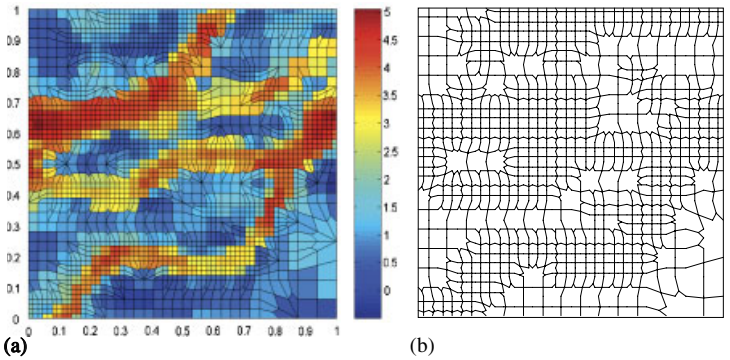

Figure 10. (a) Permeability upscaled to dual grid (CVD), primal grid also shown; and (b) Control-volume dual grid.

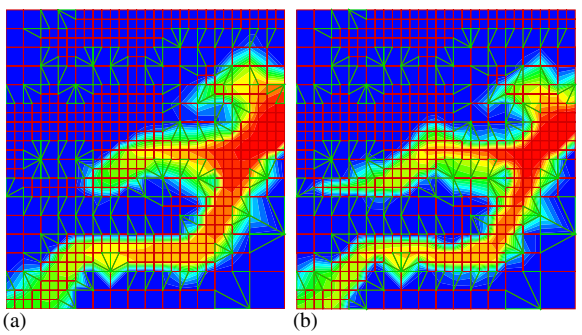

Figure 11. (a) 1st Order CVFE; and (b) 1st Order CVD.

The results obtained with the higher-order CVFE scheme and higher-order CVD scheme are shown in Figures 12(a) and (b) respectively. Both higher order methods show distinct improvements in results compared to their lower order counter parts above. However, while the higher-order CVFE

DOI: 10.1002/fld

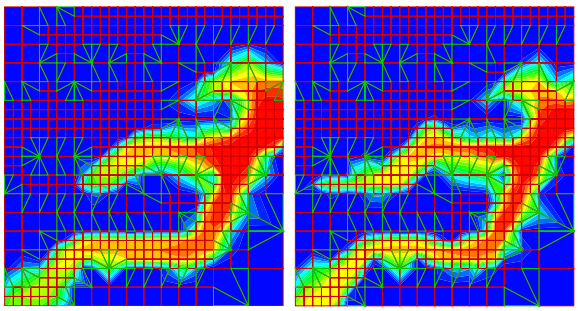

Figure 12. (a) Higher-order CVFE; and (b) higher-order CVD.

scheme improves the first order CVFE result, the higher-order CVD scheme yields the sharpest flow resolution. The CVD results show the benefits of coupling a higher-order convective flux approximation together with continuous Darcy-flux approximation for modelling two-phase flow in a heterogeneous medium on unstructured grids.

7. CONCLUSIONS

A novel higher-order convective flux approximation is coupled with consistent and efficient continuous Darcy flux approximations. The coupling leads to new schemes for reservoir simulation on structured and unstructured grids in two dimensions.

Comparisons for two-phase flow are presented with current methods in reservoir simulation and with the standard control-volume finite element CVFE scheme using exactly the same number of degrees of freedom as the new schemes. The comparisons demonstrate the benefits of the new higher-order CVD schemes both in terms of front resolution with significant reduction in unstructured grid orientation together with improved medium discontinuity resolution.

The CVFE scheme is observed to have an inherent tendency to average flow effects in the presence of rapid changes in permeability on grids of finite level. While the higher-order CVFE scheme improves front resolution compared to the first-order CVFE scheme, the higher-order CVFE scheme cannot compensate for loss of crucial Darcy flux information that occurs as a consequence of the CVFE formulation.

The test cases show the fundamental advantages of the higher-order CVD scheme (for multi-phase flow) both in terms of improved convective front resolution and the scheme's ability to detect rapid changes in permeability and yield consistent flow behaviour.

ACKNOWLEDGEMENT

Support of EPSRC grant GR/S70968/01 is gratefully acknowledged.

REFERENCES

1. Aziz K, Settari A. *Petroleum Reservoir Simulation*. Applied Science Publishers: London, 1979.
2. Bear J. *Dynamics of Fluids in Porous Media*. American Elsevier: New York, 1972.

DOI: 10.1002/fld

3. Bell JB, Colella P, Trangenstein JA. Higher order Godunov methods for general systems of hyperbolic conservation laws. *Journal of Computational Physics* 1989; **82**:362–397.
4. Blunt MJ, Rubin B. Implicit flux-limiting schemes for petroleum reservoir simulation. *Journal of Computational Physics* 1992; **102**:194–210.
5. Edwards MG, Christie MA. Dynamically adaptive Godunov schemes with renormalization for reservoir simulation SPE 25268. *Proceedings*: *Twelfth SPE Reservoir Simulation Symposium*, New Orleans, Louisiana, U.S.A., 28 February–3 March 1993; 413–422.
6. Durlofsky LJ. A triangle based mixed finite element finite volume technique for modeling two phase flow through porous media. *Journal of Computational Physics* 1993; 252–266.
7. Edwards MG. A higher order Godunov scheme coupled with dynamic local grid refinement for flow in a porous medium. *Computer Methods in Applied Mechanics and Engineering* 1996; **131**:287–308.
8. Edwards MG. Cross-flow, tensors and finite volume approximation with deferred correction. *Computer Methods in Applied Mechanics and Engineering* 1998; **151**:143–161.
9. Thiele M, Edwards MG. Physically based higher order Godunov schemes for compositional simulation. *Proceedings*: *SPE Reservoir Simulation Symposium*, *Paper 66403*, Houston, TX, U.S.A., 11–14 February 2001.
10. Edwards MG. Non-upwind versus upwind schemes for hyperbolic conservation laws in porous media. *Proceedings*: *SPE Reservoir Simulation Symposium*, *Paper 93691*, Houston, TX, U.S.A., 31 January–2 February 2005.
11. Edwards MG. Symmetric positive definite general tensor discretization operators on unstructured and flow based grids. *Proceedings*: *ECMOR VIII*, *8th European Conference on the Mathematics of Oil Recovery*, Frieberg, Germany, 3–6 September 2002.
12. Edwards MG. Unstructured, control-volume distributed, full-tensor finite volume schemes with flow based grids. *Computational Geosciences* 2002; **6**:433–452.
13. Edwards MG. Split full tensor discretization operators for structured and unstructured grids in three dimensions. *SPE 66358 Proceedings*: *SPE Reservoir Simulation Symposium*, Houston, Texas, 11–14 February 2001.
14. Edwards MG. M-matrix flux splitting for general full tensor discretization operators on structured and unstructured grids. *Journal of Computational Physics* 2000; **160**:1–28.
15. Edwards MG. Simulation with a full-tensor coefficient velocity field recovered from a diagonal tensor solution. *SPE Journal* 2000; **5**:387–393.
16. Edwards MG, Rogers CF. Finite volume discretization with imposed flux continuity for the general tensor pressure equation. *Computational Geosciences* 1998; **2**:259–290.
17. Aavatsmark I. Introduction to multipoint flux approximation for quadrilateral grids. *Computers and Geosciences* 2002; **6**:405–432.
18. Aavatsmark I, Barkve T, Mannseth T. Control-volume discretization methods for 3d quadrilateral grids in inhomogeneous, anisotropic reservoirs. *SPE Reservoir Simulation Symposium*, Dallas, TX, U.S.A., 1997.
19. Aavatsmark I, Barkve T, Bøe Ø, Mannseth T. Discretization on unstructured grids for inhomogeneous, anisotropic media. Part 1. Methods. *SIAM Journal on Scientific Computing* 1998; **19**:1700–1716.
20. Aavatsmark I, Barkve T, Bøe Ø, Mannseth T. Discretization on unstructured grids for inhomogeneous, anisotropic media. Part II. Results. *SIAM Journal on Scientific Computing* 1998; **19**:1717–1736.
21. Verma S, Aziz K. A control volume scheme for flexible grids in reservoir simulation. *SPE 37999*, *14th SPE Reservoir Simulation Symposium*, Dallas, Texas, U.S.A., 8–11 June 1997; 215–227.
22. Lee SH, Durlofsky LJ, Lough MF, Chen W. Finite difference simulation of geologically complex reservoirs with tensor permeabilities. *SPE 38002 1997*, *SPE Reservoir Simulation Symposium*, Dallas, TX, U.S.A.
23. Lee SH, Tchelepi H, DeChant LJ. Implementation of a flux continuous finite difference method for stratigraphic hexahedron grids. *Paper SPE 51901 Proceedings*: *SPE Reservoir Simulation Symposium*, Houston, Texas, U.S.A., 14–17 February 1999.
24. Raviart RA, Thomas JM. *A Mixed Finite Element method for Second Order Problems*. Lecture Notes in Mathematics, vol. 606. Springer: New York, 1977; 292–315.
25. Russel TF, Wheeler MF. Finite element and finite difference methods for continuous flows in porous media. In *Mathematics of Reservoir Simulation* (Chapter 2), Ewing RD (ed.), Frontiers in Applied Mathematics. SIAM: Philadelphia, PA, 1983; 35–106.
26. Farmer CL, Heath DE, Moody RO. *A global optimization approach to grid generation. 11th SPE Reservoir Simulation Symposium*, Anaheim, CA, U.S.A., 17–20 February 1991; 341–350.
27. Arbogast T, Wheeler MF, Yotov I. Mixed finite elements for elliptic problems with tensor coefficients as cell centered finite differences. *SIAM Journal on Numerical Analysis* 1997; **34**(2):828.

DOI: 10.1002/fld

28. Russell TF. Relationships among some conservative discretization methods. In *Numerical Treatment of Multiphase Flows in Porous Media*, Chen Z *et al*. (ed.), Lecture Notes in Physics, vol. 552. Springer: Heidelberg, 2000; 267–282.
29. Forsyth P. A control-volume finite element method for local mesh refinement in thermal reservoir simulation. *SPERE* 1990; 561.
30. Pal M, Edwards MG, Lamb AR. Convergence study of a family of flux-continuous, finite schemes for the general tensor pressure equation. *International Journal for Numerical Methods in Fluids*, submitted.
31. Edwards MG. Control-volume distributed sub-cell flux schemes for unstructured and flow based grids. *SPE Reservoir Simulation Symposium*, Houston, Texas, U.S.A., 3–5 February 2003.
32. Eigestad GT, Klausen RA. On convergence of multi-point flux approximation o-method; numerical experiment for discontinuous permeability. *Numerical Methods for Partial Differential Equations*, submitted.
33. van Leer B. Towards the ultimate conservative difference scheme V. A sequel to Godunov's method. *Journal of Computational Physics* 1979; **32**:101–136.
34. Jameson A. Artificial diffusion, upwind biasing, limiters and their effect on accuracy and multigrid convergence in transonic and hypersonic flows. *AIAA 93-3359*, 1993.
35. Lyra P, Morgan K. A review and comparative study of upwind biased schemes for compressible flow computation. Part III: Multidimensional extension on unstructured grids. *Archives of Computational Methods in Engineering* 2002; **9**(3):207–256.
36. Sweby P. High resolution schemes using flux limiters for hyperbolic conservation laws. *SIAM Journal on Numerical Analysis* 1984; **21**:995–1011.
37. Godlewski E, Raviart P. Numerical approximation of hyperbolic systems of conservation laws. *Applied Mathematical Science*, vol. 118. Springer: New York, 1996.
38. Shu CW, Osher S. Efficient implementation of essentially non-oscillatory shock capturing schemes. *Journal of Computational Physics* 1998; **77**:439–471.
39. Edwards MG. Higher-resolution hyperbolic-coupled-elliptic flux-continuous CVD schemes on structured and unstructured grids in 3-D. *International Journal for Numerical Methods in Fluids*, submitted.
40. Prevost M, Edwards MG, Blunt MJ. Streamline tracing on cuvilinear structured and unstructured grids. *SPE Journal* 2002.
41. Klausen R, Eigstad G. Multipoint flux approximations and finite element methods; practical aspects of discontinuous media. *ECMOR VIII Proceedings*: *9th European Conference on the Mathematics of Oil Recovery*, Cannes, France, 30 August–2 September 2004.
42. Warren JE, Price HS. Flow in heterogeneous porous media. *SPE Journal* 1961; 153–169.
43. Carey GF, Oden JT. *Finite Elements*, *A Second Course*, vol 2. Prentice-Hall: Englewood Cliffs, NJ.
44. Mao S, Journal AG. Generation of a reference petrophysical data set. *Forecasting Report, The Stanford V Reservoir. Standard Center for Reservoir*.

DOI: 10.1002/fld